

TOI-837 b is a Young Saturn-sized Exoplanet with a Massive $70 M_{\oplus}$ Core

Oscar Barragán^{1*}, Haochuan Yu¹, Alix Violet Freckelton², Annabella Meech³, Michael Cretignier¹, Annelies Mortier², Suzanne Aigrain¹, Baptiste Klein¹, Niamh K. O’Sullivan¹, Edward Gillen⁴, Louise Dyregaard Nielsen⁵, Manuel Mallorquín^{6,7}, Norbert Zicher¹,

¹ Sub-department of Astrophysics, Department of Physics, University of Oxford, Oxford, OX1 3RH, UK

² School of Physics and Astronomy, University of Birmingham, Edgbaston, Birmingham B15 2TT, UK

³ Center for Astrophysics, Harvard & Smithsonian, 60 Garden St, Cambridge, MA 02138, US

⁴ Astronomy Unit, Queen Mary University of London, Mile End Road, London E14NS, UK

⁵ University Observatory Munich, Ludwig Maximilian University, Scheinerstrasse 1, Munich D-81679, Germany

⁶ Instituto de Astrofísica de Canarias (IAC), Calle Vía Láctea s/n, 38205 La Laguna, Tenerife, Spain

⁷ Departamento de Astrofísica, Universidad de La Laguna (ULL), 38206 La Laguna, Tenerife, Spain

Accepted XXX. Received YYY; in original form ZZZ

ABSTRACT

We present an exhaustive photometric and spectroscopic analysis of TOI-837, a F9/G0 35 Myr young star, hosting a transiting exoplanet, TOI-837 b, with an orbital period of 8.32 d. Utilising data from *TESS* and ground-based observations, we determine a planetary radius of $0.82 R_J$ for TOI-837 b. Through detailed HARPS spectroscopic time series analysis, we derive a Doppler semi-amplitude of 36 m s^{-1} , corresponding to a planetary mass of $0.39 M_J$. The derived planetary properties suggest a substantial core of approximately $70 M_{\oplus}$, constituting about 60% of the planet’s total mass. This finding poses a significant challenge to existing theoretical models of core formation. We propose that future atmospheric observations with *JWST* could provide insights into resolving ambiguities of TOI-837 b, offering new perspectives on its composition, formation, and evolution.

Key words: Planets and satellites: individual: TOI-837 – Stars: activity – Techniques: radial velocities – Techniques: photometric

1 INTRODUCTION

Characterising the properties of young exoplanets ($< 1 \text{ Gyr}$) at different stages is crucial to understanding the evolution and populations of exoplanets. These planets are often elusive to detection using indirect techniques like transit and radial velocity (RV) methods, as strong stellar activity generates stellar signals that often overshadows their signals in photometric and spectroscopic data. Recently, tens of young transiting exoplanets have been discovered (e.g., Bouma et al. 2020; David et al. 2018; Hobson et al. 2021; Martioli et al. 2021; Mann et al. 2021; Rizzuto et al. 2020; Barragán et al. 2022b). This success is largely attributed to missions like *K2* (Howell et al. 2014) and the Transiting Exoplanet Survey Satellite (*TESS*; Ricker et al. 2015) that provide thousands of light curves of young stars.

After identifying a young transiting exoplanet, the next step typically involves spectroscopic observations to observe the star’s RV variations caused by the planet to measure its mass. However, separating signals from the planet and star in radial velocity data remains challenging. Gaussian Processes (GPs) have emerged as a favoured method for modelling activity-induced radial velocities, offering a flexible way to represent stochastic variations, such as the quasi-periodic stellar signals (see e.g., Aigrain & Foreman-Mackey 2023). Multiple authors have used GPs, and variations of them such as multidimensional GPs (see e.g., Rajpaul et al. 2015; Barragán et al.

2022a), to detect RV planetary signals on spectroscopic time series of active young stars (e.g., Barragán et al. 2019b, 2023; Mantovan et al. 2023; Mallorquín et al. 2023; Zicher et al. 2022). Nevertheless, although widely embraced by the community, there exists a notable concern that the GP activity model may inadvertently mask or alter potential planetary signals (see e.g., discussions in Ahrer et al. 2021; Rajpaul et al. 2021). A recent example of this comes from Suárez Mascareño et al. (2021). The authors, utilising GPs, discovered that the planets orbiting the young V 1298 Tau exhibited significantly higher density than anticipated. However, these detections have been challenged by the exoplanet community. Blunt et al. (2023) suggested that Suárez Mascareño et al. (2021)’s detections may have been affected by over-fitting, thereby questioning the reliability of their RV Doppler detections. This is crucial, especially in cases where the measurements are in tension with models.

Bouma et al. (2020, hereafter B20) reported the discovery and validation of the young transiting exoplanet around TOI-837. The star is a young ($\sim 35 \text{ Myr}$) F9/G0 dwarf star in the southern open cluster IC 2602. TOI-837’s main identifiers and parameters are given in Table 1. They used *TESS* cycle 1, the GAIA mission, multi-band photometry and spectroscopic observations to validate the planetary nature of a transit signal. The transit object corresponds to a planet with a radius of $\sim 0.77 R_J$ and a period of 8.32 d. In this manuscript, we present a spectroscopic follow-up and exhaustive analysis of TOI-837, to characterise further the nature of TOI-837 b. This paper is structured as follows: The photometric and spectroscopic data of TOI-837 are detailed in Section 2. The analytical methods applied

* oscar.barragan@physics.ox.ac.uk

Table 1. Main identifiers and parameters for TOI-837.

Parameter	Value	Source
<i>Main identifiers</i>		
Gaia DR3	5251470948229949568	Gaia Collaboration (2020)
TYC	8964-17-1	Høg et al. (2000)
2MASS	J10280898-6430189	Cutri et al. (2003)
Spectral type	F9/G0	Bouma et al. (2020)
<i>Equatorial coordinates, proper motion, and parallax</i>		
α (J2000.0)	10 28 08.9903	Gaia Collaboration (2020)
δ (J2000.0)	-64 30 18.9364	Gaia Collaboration (2020)
μ_α (mas yr ⁻¹)	-17.912 ± 0.014	Gaia Collaboration (2020)
μ_δ (mas yr ⁻¹)	11.490 ± 0.014	Gaia Collaboration (2020)
π (mas)	7.0108 ± 0.0124	Gaia Collaboration (2020)
Distance (pc)	142.74 ± 0.25	Gaia Collaboration (2020)
<i>Magnitudes</i>		
B	11.12 ± 0.06	Høg et al. (2000)
V	10.64 ± 0.05	Høg et al. (2000)
Gaia	10.3598 ± 0.0028	Gaia Collaboration (2020)
J	9.392 ± 0.030	Cutri et al. (2003)
H	9.108 ± 0.038	Cutri et al. (2003)
Ks	8.933 ± 0.026	Cutri et al. (2003)
W1	8.901 ± 0.023	AllWISE
W2	8.875 ± 0.021	AllWISE
W3	8.875 ± 0.020	AllWISE
<i>Stellar parameters</i>		
T_{eff} (K)	5995 ± 79	This work
$\log g_{\text{spec}}$ (cgs)	4.61 ± 0.08	This work
[Fe/H]	0.01 ± 0.04	This work
$v \sin i$ (km s ⁻¹)	16.8 ± 0.1	This work
Mass (M_\odot)	1.142 ^{+0.008} _{-0.011}	This work
Radius (R_\odot)	1.052 ^{+0.012} _{-0.007}	This work
Luminosity (L_\odot)	1.34 ^{+0.06} _{-0.12}	This work
Density (g cm ⁻³)	1.38 ^{+0.02} _{-0.04}	This work
$\log g_{\text{isoc}}$ (cgs)	4.453 ^{+0.003} _{-0.008}	This work
Age (Myr)	35 ⁺⁷ ₋₄	This work
$P_{\text{rot,max}}$ (d)	3.17 ± 0.04	This work

to this data are outlined in Section 3. A discussion of the findings is provided in Section 4, and the paper concludes with a summary of the key outcomes in Section 5. This manuscript is part of a series of papers under the project *GPRV: Overcoming stellar activity in radial velocity planet searches* funded by the European Research Council (ERC, P.I. S. Aigrain).

2 TOI-837 DATA

2.1 TESS data

TOI-837 (TIC 460205581) was observed by the *TESS* mission on cycles 1, 3 and 5. During cycle 1, TOI-837 was observed in Sectors 10 and 11 from 2019 March 26 to 2019 May 20 with a 2 min cadence. The *TESS* Science Processing Operations Center (SPOC; Jenkins et al. 2016) transit search (Jenkins 2002; Jenkins et al. 2010, 2020) discovered a transiting signal with a period of 8.3 d in TOI-837's

light curve. This was announced in the *TESS* SPOC Data Validation Report (DVR; Twicken et al. 2018; Li et al. 2019) and designated by the *TESS* Science Office as *TESS* Object of Interest (TOI; Guerrero et al. 2021) TOI-837.01 (hereafter TOI-837 b). B20 used this cycle 1 data, together with ancillary observations to validate the planetary nature of the TOI-837 b signal.

During cycles 3 and 5, TOI-837 was reobserved in Sectors 37 and 38 (from 2021 April 02 to 2021 May 26, with 2 min cadence) and Sectors 63 and 64 (2023 Mar 10 to 2023 May 04, with 20 s cadence), respectively. We downloaded the Presearch Data Conditioning Simple Aperture Photometry (PDCSAP; Smith et al. 2012; Stumpe et al. 2012, 2014) light curves for TOI-837 from the Mikulski Archive for Space Telescopes (MAST). Figure 1 shows the TOI-837's light curves for all the three *TESS* cycles. TOI-837 will be re-observed by *TESS* in Sector 90 during the first semester of 2025.

To perform the transit analysis we flattened the *TESS* light curves (see Sect. 3.2). The *TESS* light curves for TOI-837 exhibit variations outside of transits, possibly due to stellar or instrumental variability. The *TESS* light curves were detrended using the open-source code *citlalicue* (Barragán et al. 2022a). In essence, *citlalicue* employs GPs, as implemented in *george* (Ambikasaran et al. 2015), to model light curve fluctuations outside of transits. We provided *citlalicue* with normalised light curves and the ephemeris for the transit signal. To focus on removing low-frequency signals, we used data binned at 3-hour intervals and masked all transits when fitting the GP with a Quasi-Periodic kernel (as in Ambikasaran et al. 2015). We applied an iterative maximum Likelihood optimisation coupled with a 5-sigma clipping technique to identify the best model for light curve variations outside of transits. Subsequently, we divided the entire light curves based on this model, resulting in a flattened curve showing only transit signals. It is worth noting that each *TESS* cycle was detrended individually. The detrended light curves for all *TESS* cycles are presented in Figure 1.

2.2 Ground-based photometric data

B20 performed multi-band ground based follow-up of TOI-837. For full details on the acquisition and reduction we refer the reader to that paper. Four transit events were monitored using the 0.36-meter telescope at El Sauce Observatory, situated in Chile's Río Hurtado Valley. The data collection occurred during specific nights: the Cousins-R band was used on April 1 and 26 of 2020, the Cousins-I band on May 21, 2020, and the Johnson-B band on June 14, 2020. TOI-837 was also observed by the Antarctic Search for Transiting Exoplanets (ASTEP) telescope at the Concordia base on the Antarctic Plateau, on the dates of May 12, May 29, June 14, and June 23 of 2020. We downloaded all these public data to include them in our analyses.

2.3 HARPS spectroscopic observations

We acquired 75 high-resolution ($R \approx 115\,000$, wavelength range of 380 to 690 nm) spectra of TOI-837 with the High Accuracy Radial velocity Planet Searcher (HARPS; Mayor et al. 2003) spectrograph. The instrument is mounted at the 3.6 m ESO telescope at La Silla Observatory, Chile.

The observations were carried out between October 03 2022 and January 16 2023, as part of the observing program 0110.C-4341(A) (PI: Yu). The typical exposure time per observation was 1800 s, except for the observations before October 25 where the exposure time was set to 900 s. This produced spectra with a typical signal-to-noise (S/N) of 50 (30 for the 900s exposures) at 550 nm.

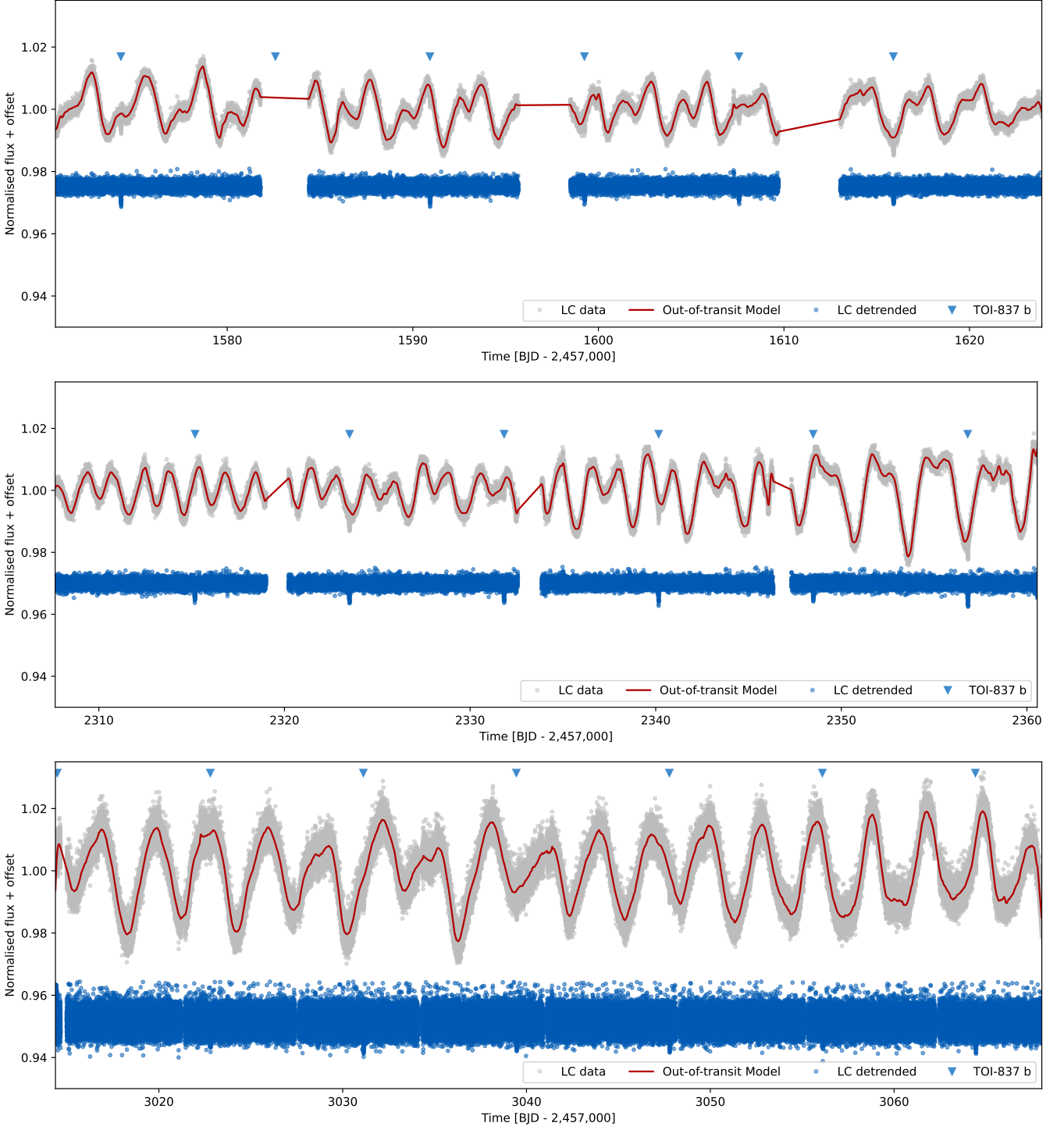


Figure 1. *TESS* light curves for TOI-837 in cycles 1, 3 and 5 (from top to bottom). *TESS* data are shown with grey points with the out-of-transit variability model over-plotted in red. The resulting flattened light curve is presented with blue points. TOI-837’s transit positions are marked with a blue triangle. All plots have the same y-range to ease comparison of data and signals.

We post-processed the 1-D spectra produced by the official data reduction software (DRS). All the spectra $S(\lambda_i, t)$ were first continuum normalised by **RASSINE** (Cretignier et al. 2020b), an upper envelope method fitting the spectra continua $C(\lambda_i, t)$. The normalised spectra time series $f(\lambda_i, t) = S(\lambda_i, t)/C(\lambda_i, t)$ was then post-processed by YARARA (Cretignier et al. 2021). Given the lim-

ited S/N of the observations, we restricted the cleaning by YARARA to cosmic rays and tellurics which are the only notable features at such a level of flux precision. From this step onwards, four observations were rejected by YARARA based on an anomalous number of detected outliers. Those spectra were all very low S/N observations (< 25). Once spectra were corrected of systematics, the normalised

flux spectra $f(\lambda_i)$ were scaled back to absolute flux units spectra $S(\lambda_i)$ by using a reference continuum¹ $C_{\text{ref}}(\lambda)$ where the bolometric flux of the spectra was preserved during the scaling:

$$S(\lambda_i, t) = f(\lambda_i, t) \cdot C_{\text{ref}}(\lambda_i) \cdot \frac{\sum_i C(\lambda_i)}{\sum_i C_{\text{ref}}(\lambda_i)}$$

This step is equivalent in practice to the colour correction usually performed on the order-by-order CCFs to remove any dependency with airmass or weather condition (Lovis 2007; Cretignier 2022). We extracted the RVs by a Gaussian fit on CCFs obtained using the G2 mask of the HARPS DRS since for fast-rotating stars, the empirical line list (see e.g., Cretignier et al. 2020a) obtained from the observations could be imperfect due to a large number of blends.

Our HARPS RV measurements have a typical error of 10 m s^{-1} and a RMS of 100 m s^{-1} . The full width at half maximum (FWHM) of the CCF shows a consequent broadening with a value around FWHM $\sim 26 \text{ km s}^{-1}$ in agreement with the fast rotation rate of the star (see Sect. 3.1). Table 2 lists the extracted HARPS RVs, FWHM, Bisector span (BIS), calcium lines S-index (S_{HK}), and Hydrogen-alpha (H_α) time series.

2.3.1 Periodograms

As a first check to test the information contained in our HARPS spectroscopic time series, we ran a General Lomb-Scargle (GLS; Zechmeister & Kürster 2009) periodogram on them. Figure 2 shows the periodogram of all the time series. We can see that all of the spectroscopic time series peak around 3 and 1.5 d, which correspond to the rotational period of the star and its first harmonic. The peaks at the stellar rotation period and its first harmonic suggest the presence of active regions on the stellar surface (e.g., Aigrain et al. 2012). No substantial peak corresponding to the orbital period of TOI-837 b is evident in the raw RVs.

3 DATA ANALYSIS

3.1 Stellar parameters

3.1.1 Atmospheric parameters

We used the HARPS spectra to derive the atmospheric parameters of TOI-837. As this star is a fast rotator, we analysed the spectra using spectral synthesis. Two different methods were employed, FASMA-synthesis² and PAWS³, as well as two different sets of spectra, the DRS spectra and the YARARA-processed spectra (see Sect. 2.3). Each set of spectra was shifted in the lab frame and co-added and the analyses were performed on this co-added spectrum.

FASMA-synthesis made use of the MARCS atmospheric models (Gustafsson et al. 2008) and the radiative transfer code MOOG⁴. Micro- and macroturbulent velocities were calculated through the calibration relations mentioned in Tsantaki et al. (2013) and Doyle et al. (2014), respectively. More details on this method can be found in Tsantaki et al. (2020).

PAWS uses the functionalities from iSPEC (Blanco-Cuaresma 2019) and is described in more detail in Freckleton et al. (2024). We used the Kurucz atmospheric models in our analysis (Kurucz 1993) and skipped the initial step of the equivalent width analysis

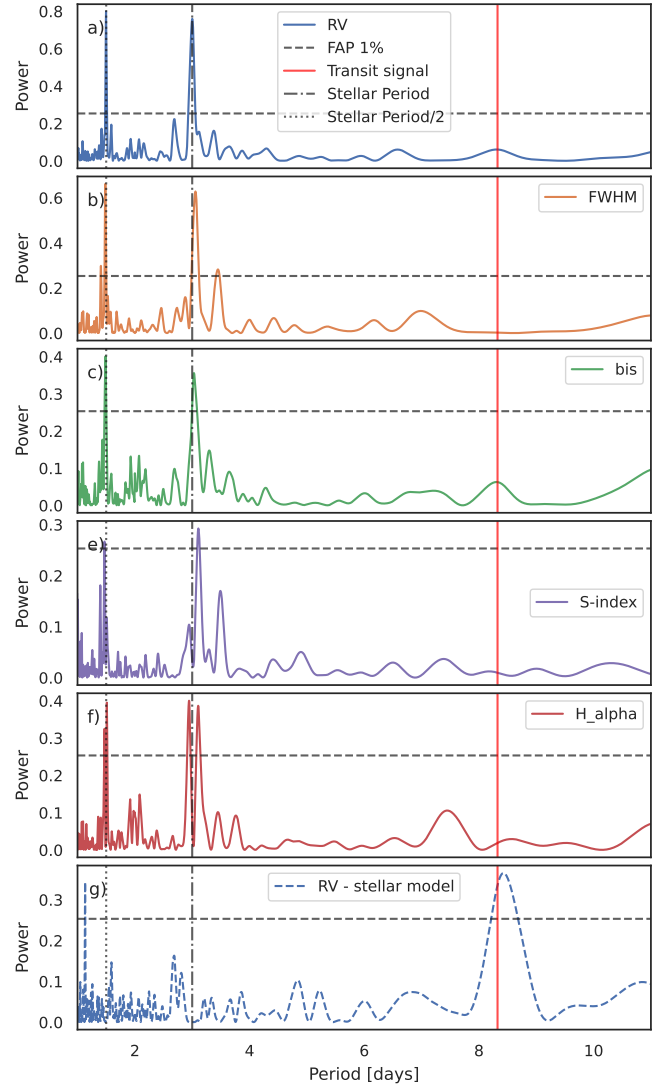


Figure 2. Lomb-Scargle periodograms of the spectroscopic time series. Panels a) to f) show the results of the time series as extracted in Sect. 2.3. Panel g) shows a Lomb-Scargle periodogram applied to the RVs once the stellar model has been removed (see Sect. 3.4). The horizontal dashed line marks the 1% False Alarm Probability (FAP). The dot-dashed and dotted black lines denote the stellar rotation period and its first harmonic, respectively; the vertical red line denotes the orbital period of TOI-837 b.

as this is less reliable for fast rotators where the spectral lines are broadened.

These four analyses provided values for the effective temperature, the surface gravity, the metallicity, and the projected rotational velocity. All values are in agreement with their 1-sigma errors. For our adopted parameters, listed in Table 1, we choose to take a weighted average of all the results. The high value of the projected rotational velocity (16.8 km/s) confirms the fast-rotating nature of TOI-837. All other parameters are close to Solar values.

3.1.2 Mass, radius, and age

To calculate the fundamental stellar parameters, we made use of the isochrones (Morton 2015) package. Our stellar models came

¹ Sometimes referred as a “reference colour”.

² <https://github.com/MariaTsantaki/FASMA-synthesis>

³ <https://github.com/alixviolet/PAWS>

⁴ <https://www.as.utexas.edu/~chris/moog.html>

Table 2. HARPS spectroscopic measurements. The full version of this table is available in a machine-readable format as part of the supplementary material.

Time BJD _{TDB} - 2 470 000	RV km s ⁻¹	σ_{RV} km s ⁻¹	FWHM km s ⁻¹	σ_{FWHM} km s ⁻¹	BIS km s ⁻¹	σ_{BIS} km s ⁻¹	S_{HK}	$\sigma_{S_{HK}}$	H α	$\sigma_{H\alpha}$	S/N (550 nm)
2855.882062	0.0634	0.0160	24.0112	0.0521	-0.0708	0.0216	0.0386	0.0242	0.3979	0.0039	27
2859.873603	-0.0075	0.0155	23.8725	0.0505	-0.0957	0.0210	0.0811	0.0238	0.3918	0.0035	29
2860.880897	0.0386	0.0206	23.7631	0.0671	-0.4361	0.0278	0.0255	0.0347	0.3972	0.0048	23
2861.882173	0.1588	0.0172	24.0269	0.0560	-0.3255	0.0232	0.0683	0.0302	0.3954	0.0041	26
2863.879982	0.0442	0.0152	23.9185	0.0493	-0.3695	0.0204	-0.0254	0.0214	0.3899	0.0031	32
...											

from the MESA Isochrones and Stellar Tracks (MIST - [Dotter 2016](#)) and we used the nested sampler `MultiNest` ([Feroz et al. 2019](#)) for our likelihood analysis. As input data, we used the photometric magnitudes B, V, J, H, Ks, W1, W2, W3, the Gaia DR3 parallax, and the spectroscopically derived effective temperature and metallicity. In a similar way as described in [Mortier et al. \(2020\)](#), we ran the code four times, each time changing the spectroscopic input to the individually obtained results and keeping the other data the same. Narrow bounds were set on the stellar age, between 30 and 46 Myr, following [B20](#), which helps constrain the stellar mass given strong correlations between mass and age for young stars.

After checking that all parameters from the individual runs agreed within errors, the final parameters and errors, listed in Table 1, were obtained from the median and 16th/84th percentile of the combined posterior distributions of the four runs. The mass and radius values are, unsurprisingly, close to Solar values. From these, we can recalculate a much more precise value of the surface gravity. It is lower than, but consistent with, the spectroscopically derived surface gravity. Using the stellar radius and the projected rotational velocity, we can furthermore also place an upper limit on the stellar rotation period. We find that the rotation period has a maximum value of 3.17 ± 0.04 d. This is fully compatible with the values obtained with *TESS* and spectroscopic time series (see Sect. 3.3).

3.2 Transit analysis

For all the subsequent planet analyses we used the code `pyaneti` ([Barragán et al. 2019a; Barragán et al. 2022a](#)). In all our runs we sample the parameter space with 250 walkers using the Markov chain Monte Carlo (MCMC) ensemble sampler algorithm implemented in `pyaneti` ([Barragán et al. 2019a; Foreman-Mackey et al. 2013](#)). The posterior distributions are created with the last 5000 iterations of converged chains. We thinned our chains by a factor of 10 giving a distribution of 125 000 points for each sampled parameter.

To speed up the transit modelling, we only model data chunks spanning a maximum of three hours on either side of each transit mid-time. *TESS* and ground-based photometry were acquired with short cadence (< 2 min). Therefore we can assume that this data can be described by instantaneous evaluations of the transit models and we do not need model re-sampling (see e.g., [Gandolfi et al. 2018](#)). In total we have six different photometric data sets named: *TESS* 2 min data (cycles 1 and 3), *TESS* 25s data (cycle 5), *ASTEP*, and *El Sauce R, I, and B* bands.

To model the transits of TOI-837 b, we need to set priors for the following set of parameters: time of mid-transit, T_0 ; orbital period, P_{orb} ; orbital eccentricity, e and angle of periastron, ω using the polar parametrisation $\sqrt{e} \cos \omega_\star$ and $\sqrt{e} \sin \omega_\star$; scaled planetary radius R_p/R_\star ; the stellar density, ρ_\star ; and the limb darkening parameters q_1 and q_2 for each band (following [Mandel & Agol 2002; Kipping](#)

[2013](#), models and parametrisations). We assume a black object transit and we sample for a single R_p/R_\star for all bands ([B20](#) showed that there is no variation of R_p/R_\star in different bands). The scaled semi-major axis, a/R_\star , is recovered from ρ_\star and Kepler's third law (see e.g., [Winn 2010](#)). The model also includes photometric jitter term per data set to penalise the likelihood. We start by assuming that the orbit is circular, so we fix $\sqrt{e} \cos \omega_\star = \sqrt{e} \sin \omega_\star = 0$. For the rest of parameters we set wide informative uniform priors as listed in Table 3.

To start our transit analysis, it is worth mentioning that TOI-837 b's transit looks V-shaped, indicating that the transit could be grazing (where the grazing condition is given when $b > 1 - R_p/R_\star$). [B20](#) reported $b = 0.94 \pm 0.013$ and $R_p/R_\star = 0.08 \pm 0.01$, suggesting that the transit is either grazing or nearly grazing. We note that [B20](#) performed this analysis using the available data at the time: *TESS* cycle 1 and the ground-based data. We performed an analysis using exactly this data set, and we obtained fully consistent results of $b = 0.923^{+0.019}_{-0.011}$ and $R_p/R_\star = 0.079^{+0.006}_{-0.003}$. The small differences with [B20](#) can be explained by the different ways to deal with the detrending and/or different parametrisations.

We then repeated the analysis including the new data of the *TESS* cycles 3 and 5. We obtained more precise values of $b = 0.921^{+0.014}_{-0.009}$ and $R_p/R_\star = 0.080^{+0.004}_{-0.002}$. These values are still consistent with a grazing transit. Figure 3 shows a correlation plot between b , ρ_\star , and R_p/R_\star . We can see that the grazing condition covers only the low probability tail of the posterior distribution. Therefore, we are able to put strong constraints on the inferred planetary radius.

It is also worth mentioning that the stellar density recovered from the transit analysis, $\rho_\star = 1.58 \pm 0.17 \text{ g cm}^{-3}$, is fully consistent with the stellar parameters derived in Section 3.1. This suggests that the planetary orbit is nearly circular. To test this further, we performed another transit analysis where we used a Gaussian prior on the stellar density using the value in Table 1. We also sample for the orbit eccentricity using the polar parametrisation $\sqrt{e} \cos \omega_\star$ and $\sqrt{e} \sin \omega_\star$. We inferred $\sqrt{e} \cos \omega_\star = 0.08^{+0.12}_{-0.15}$ and $\sqrt{e} \sin \omega_\star = 0.10^{+0.39}_{-0.35}$ that relates to an eccentricity of $e = 0.10^{+0.17}_{-0.06}$. These results are consistent with a nearly circular orbit for TOI-837 b. It is also worth mentioning that the model with a circular orbit is strongly preferred over the model with eccentricity with a difference of Akaike Information Criterion (ΔAIC) of 52. We then conclude that the photometric data strongly prefers a model assuming a circular orbit. Figure 4 shows TOI-837 b's transits for the different data sets with the respective inferred models.

3.3 Characterising the stellar signal

Because of its youth, TOI-837 has strong stellar signals in its light curve and RVs time series. We performed several analyses of the

Table 3. Modelled and derived parameters for TOI-837 b.

Parameter	Prior ^(a)	Final value ^(b)
TOI-837 b's parameters		
Orbital period P_{orb} (days)	$\mathcal{U}[8.3239, 8.3259]$	8.3249114 ± 0.0000037
Transit epoch T_0 (BJD _{TDB} - 2 470 000)	$\mathcal{U}[2356.77, 2356.87]$	2356.81402 ± 0.00025
Scaled planet radius R_p/R_\star	$\mathcal{U}[0.0, 0.2]$	$0.0798^{+0.0030}_{-0.0021}$
Impact parameter, b	$\mathcal{U}[0, 1.2]$	$0.918^{+0.017}_{-0.008}$
$\sqrt{e} \cos \omega_\star$	$\mathcal{F}[0]$	0
$\sqrt{e} \sin \omega_\star$	$\mathcal{F}[0]$	0
Doppler semi-amplitude, K (m s ⁻¹)	$\mathcal{U}[0, 100]$	$36.2^{+6.8}_{-6.3}$
GP hyperparameters		
GP Period P_{GP} (days)	$\mathcal{U}[2.5, 3.5]$	$2.998^{+0.010}_{-0.012}$
λ_p	$\mathcal{U}[0.1, 5]$	$0.39^{+0.20}_{-0.13}$
λ_e (days)	$\mathcal{U}[1, 100]$	48^{+23}_{-17}
A_{RV} (m s ⁻¹)	$\mathcal{U}[0, 1000]$	157^{+105}_{-49}
Other parameters		
Stellar density ρ_\star (g cm ⁻³)	$\mathcal{U}[0.5, 2.5]$	1.61 ± 0.15
TESS Parameterised limb-darkening coefficient q_1	$\mathcal{U}[0, 1]$	$0.875^{+0.091}_{-0.173}$
TESS Parameterised limb-darkening coefficient q_2	$\mathcal{U}[0, 1]$	$0.120^{+0.146}_{-0.086}$
El Sauce-R Parameterised limb-darkening coefficient q_1	$\mathcal{U}[0, 1]$	$0.44^{+0.18}_{-0.14}$
El Sauce-R Parameterised limb-darkening coefficient q_2	$\mathcal{U}[0, 1]$	$0.41^{+0.30}_{-0.28}$
El Sauce-I Parameterised limb-darkening coefficient q_1	$\mathcal{U}[0, 1]$	$0.53^{+0.24}_{-0.21}$
El Sauce-I Parameterised limb-darkening coefficient q_2	$\mathcal{U}[0, 1]$	$0.28^{+0.31}_{-0.20}$
El Sauce-B Parameterised limb-darkening coefficient q_1	$\mathcal{U}[0, 1]$	$0.42^{+0.20}_{-0.19}$
El Sauce-B Parameterised limb-darkening coefficient q_2	$\mathcal{U}[0, 1]$	$0.35^{+0.33}_{-0.24}$
ASTEP Parameterised limb-darkening coefficient q_1	$\mathcal{U}[0, 1]$	$0.316^{+0.115}_{-0.088}$
ASTEP Parameterised limb-darkening coefficient q_2	$\mathcal{U}[0, 1]$	$0.70^{+0.19}_{-0.29}$
Jitter term $\sigma_{\text{TESS}, 2\text{min}}$ (ppm)	$\mathcal{J}[1, 5000]$	$205.4^{+75.4}_{-98.5}$
Jitter term $\sigma_{\text{TESS}, 25\text{s}}$ (ppm)	$\mathcal{J}[1, 5000]$	248^{+118}_{-145}
Jitter term σ_R (ppm)	$\mathcal{J}[1, 5000]$	1738^{+114}_{-110}
Jitter term σ_I (ppm)	$\mathcal{J}[1, 5000]$	1581^{+191}_{-192}
Jitter term σ_B (ppm)	$\mathcal{J}[1, 5000]$	731^{+478}_{-490}
Jitter term σ_{ASTEP} (ppm)	$\mathcal{J}[1, 5000]$	1311^{+63}_{-62}
HARPS offset (km s ⁻¹)	$\mathcal{U}[-0.67, 0.71]$	$0.014^{+0.085}_{-0.074}$
HARPS Jitter, σ_{HARPS} (m s ⁻¹)	$\mathcal{J}[1, 100]$	$29.6^{+4.1}_{-3.7}$
TOI-837 b's derived parameters		
Planet radius, (R_J)	...	$0.817^{+0.032}_{-0.023}$
Planet mass, (M_J)	...	$0.395^{+0.074}_{-0.069}$
Planet density, ρ_p (g cm ⁻³)	...	$0.89^{+0.20}_{-0.18}$
Scaled semi-major axis a/R_\star	...	$18.05^{+0.54}_{-0.56}$
semi-major axis a (AU)	...	$0.0883^{+0.0028}_{-0.0029}$
Orbital inclination i (deg)	...	$87.08^{+0.11}_{-0.13}$
Equilibrium temperature ^(c) T_{eq} (K)	...	998 ± 21
Transit duration τ_d (h)	...	2.000 ± 0.034
Planet surface gravity g_p (cm s ⁻²) ^(d)	...	1603^{+377}_{-340}
Planet surface gravity g_p (cm s ⁻²) ^(e)	...	1457^{+302}_{-278}
Insolation F_p (F_\oplus)	...	165^{+14}_{-13}

^a $\mathcal{F}[a]$ refers to a fixed value a , $\mathcal{U}[a, b]$ to an uniform prior between a and b , $\mathcal{N}[a, b]$ to a Gaussian prior with mean a and standard deviation b , and $\mathcal{J}[a, b]$ to the modified Jeffrey's prior as defined by Gregory (2005, eq. 16).

^b Inferred parameters and errors are defined as the median and 68.3% credible interval of the posterior distribution.

^c Assuming an albedo of zero.

^d Derived using $g_p = GM_p R_p^{-2}$.

^e Derived using sampled parameters following Southworth et al. (2007).

light curves and spectroscopic time series to analyse the time scales over which the stellar signal evolves.

3.3.1 Stellar signal in the TESS light curves

We first performed a onedimensional GP regression of the *TESS* light curves to study the behaviour of the stellar signal at the different *TESS* cycles. Since we are interested in modelling the long-term evolution

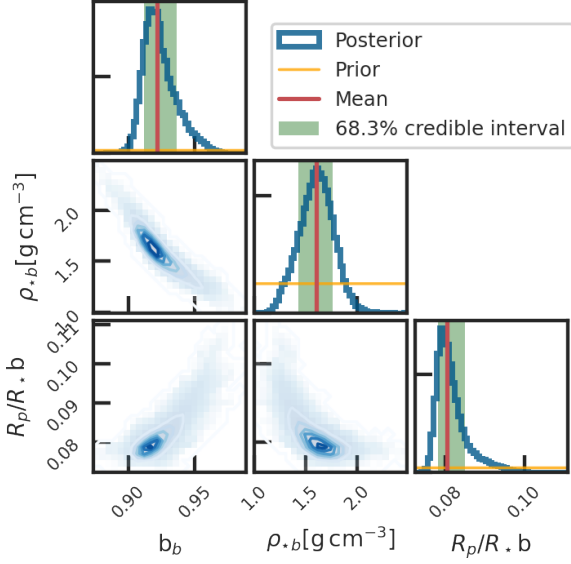


Figure 3. Correlation plot for the main parameters of the transit analysis.

of the light curve, we binned the data into 3 hour chunks and masked the transits out of the light curve.

We model the covariance between two data points at times t_i and t_j for each time-series as

$$\gamma_{1D} = A^2 \gamma_{i,j}, \quad (1)$$

where A is an amplitude term, and $\gamma_{i,j}$ is the Quasi-Periodic (QP) kernel given by

$$\gamma_{QP,i,j} = \exp \left[-\frac{\sin^2[\pi(t_i - t_j)/P_{GP}]}{2\lambda_p^2} - \frac{(t_i - t_j)^2}{2\lambda_e^2} \right], \quad (2)$$

whose hyperparameters are: P_{GP} , the GP characteristic period; λ_p , the inverse of the harmonic complexity; and λ_e , the long-term evolution timescale.

We sample 5 parameters in each run: four GP hyperparameters (A , P_{GP} , λ_e , λ_p), and a jitter term included in the Gaussian Likelihood. We set wide uniform priors for all the parameters: for λ_e we set a uniform prior between 0.1 and 100 d, for λ_p between 0.1 and 5, and for P_{GP} between 2.5 and 3.5 d. We sample the parameter space using the built-in MCMC sampler in [pyaneti](#) using the same criteria as in Sect. 3.2.

Table 4 shows the inferred P_{GP} , λ_e , and λ_p hyperparameters for all the light curves. Figure 5 shows the inferred posterior distributions for the P_{GP} , λ_e , and λ_p parameters for all the modelled time series. Figure 6 shows the *TESS* light curves with the inferred GP model. The first thing we observe is that the recovered P_{GP} is consistent within the maximum rotational period derived in Section 3.1. However, the rotational period obtained from *TESS* Cycle 1 is consistent with Cycles 3 and 5 just at 3 sigma. This could be evidence of differential rotation. This can also be caused by the relatively short evolution time-scale recovered that is smaller than the inferred period (see e.g., [Rajpaul et al. 2015](#)). We note that all the hyperparameters seem consistent between the different light curves. This is unusual for young stars given that each *TESS* cycle happens two years after another and the evolution of stellar activity can manifest as different signals that can be explained by different GP hyperparameters (e.g., [Barragán et al. 2021](#)).

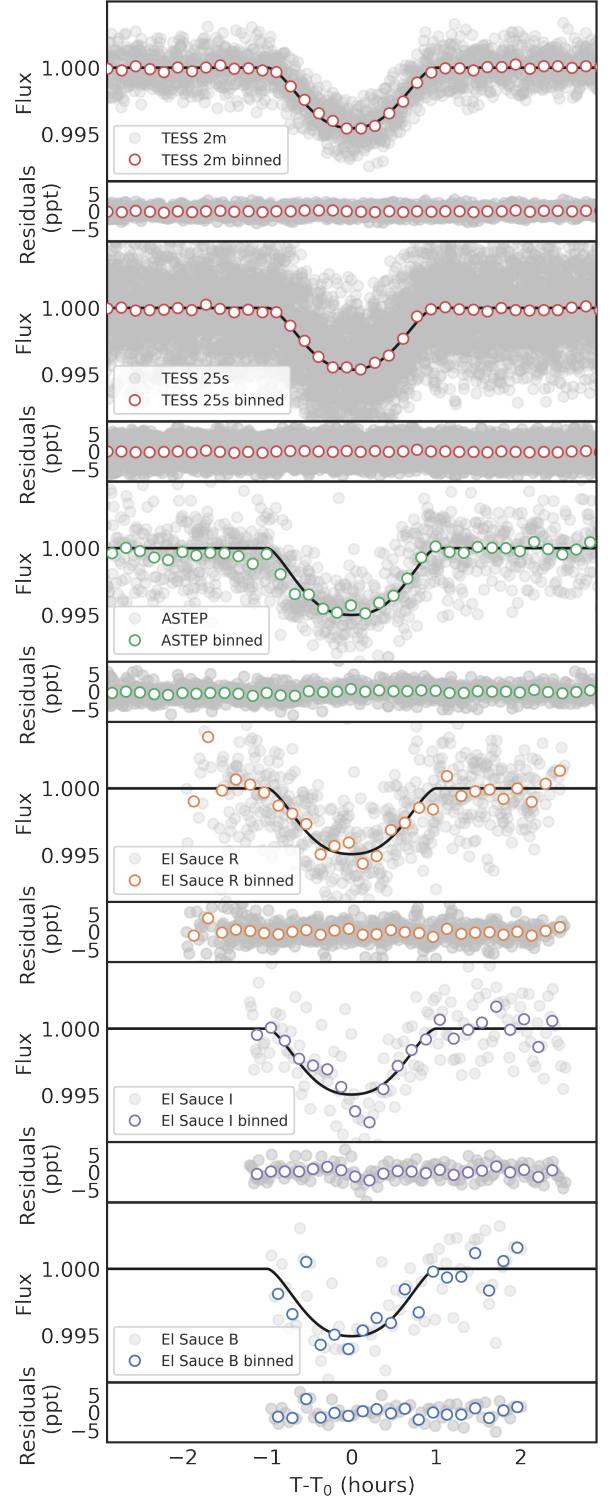


Figure 4. Phase-folded light curves of TOI-837 b for different data sets. Nominal observations are shown in light grey. Coloured circles represent 10-min binned data. Transit models are shown with a solid black line.

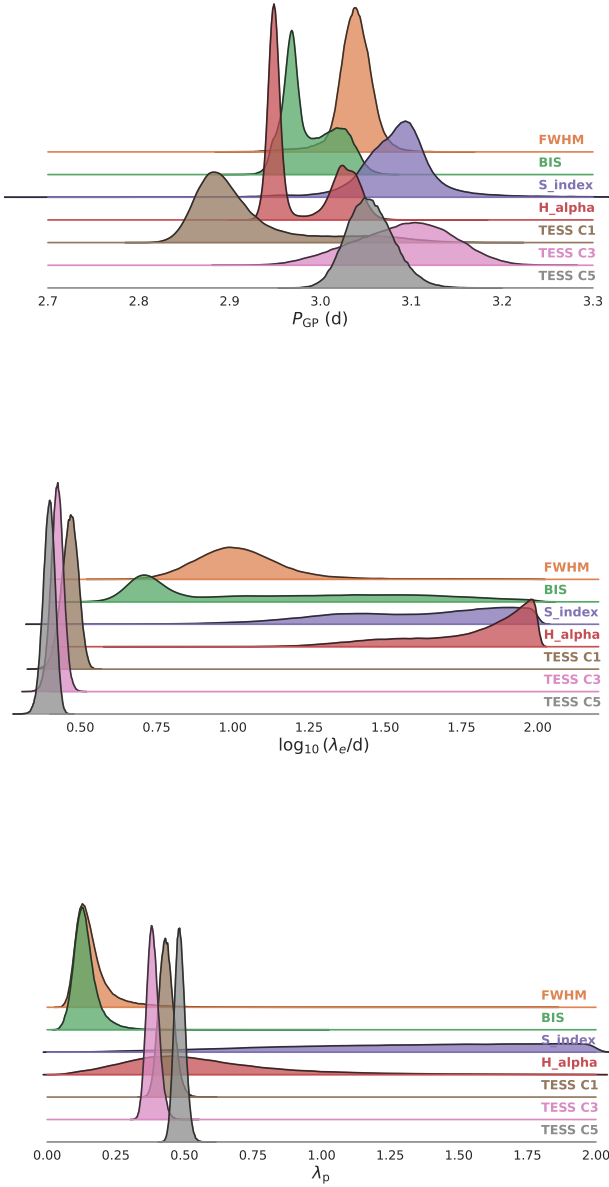


Figure 5. Posterior distributions for P_{GP} (top), $\log_{10}(\lambda_e/d)$ (middle), and λ_p (bottom). Results for FWHM (orange), BIS (green), S_{HK} (purple), H_α (red), and *TESS* cycles 1 (brown), 3 (pink), 5 (grey) are shown for each sub-panel.

3.3.2 Stellar signal in the activity indicators

We performed an individual analysis of each activity indicator as the one presented in [Barragán et al. \(2023\)](#). We analyse the FWHM, BIS, S_{HK} , and H_α spectroscopic time series. Note that, in comparison with Section 3.3.1, we are now facing a more difficult signal characterisation given that the spectroscopic time series are not as well sampled as the *TESS* light curves.

In Section 2.3.1 we show how all the spectroscopic time-series periodograms show significant peaks around 3 and 1.5 d, which are related to the stellar rotational period and its first harmonic, respectively. To better characterise the periodic signals and analyse further signal complexity, we performed a GP regression on each time series

Table 4. Recovered hyperparameters for onedimensional GP regression for different stellar time series.

Time-series	P_{GP} [d]	λ_e [d]	λ_p
<i>TESS</i> cycle 1	$2.90^{+0.07}_{-0.03}$	$2.94^{+0.18}_{-0.19}$	$0.43^{+0.03}_{-0.03}$
<i>TESS</i> cycle 3	$3.09^{+0.05}_{-0.06}$	$2.66^{+0.13}_{-0.12}$	$0.38^{+0.02}_{-0.02}$
<i>TESS</i> cycle 5	$3.05^{+0.03}_{-0.02}$	$2.50^{+0.11}_{-0.12}$	$0.48^{+0.02}_{-0.02}$
FWHM	3.04 ± 0.02	$10.3^{+4.1}_{-2.6}$	$0.15^{+0.06}_{-0.04}$
BIS Span	$2.98^{+0.05}_{-0.02}$	$11.7^{+30.4}_{-6.7}$	$0.13^{+0.04}_{-0.03}$
S_{HK}	3.09 ± 0.03	$44.3^{+35.4}_{-24.9}$	$1.35^{+0.45}_{-0.35}$
H_α	$2.95^{+0.08}_{-0.01}$	$71.8^{+20.8}_{-36.5}$	$0.51^{+0.31}_{-0.21}$

using the 1D modelling setup as the one presented in Sect. 3.3.1. We sample for 6 parameters in each run, the kernel hyperparameters (A , P_{GP} , λ_e , λ_p), an offset, and a jitter term. The priors used were uniform with the ranges: for λ_e between 0.1 and 100 d (that corresponds to the HARPS observing window), λ_p between 0.1 and 2, and for P_{GP} between 2.5 and 3.5 d.

Table 4 and Figure 5 summarise the inferred GP hyperparameters. Figure 6 shows the spectroscopic time-series data together with the inferred GP model. The first thing we note is that all activity indicators can recover a period that is consistent with the stellar rotation period. This is consistent with the results found in the periodogram analysis (even the double peak observed in the H_α periodogram is presented in the recovered posterior, see Sect. 2.3.1). We were expecting a better agreement between the hyperparameters recovered from the spectroscopic time series (see [Barragán et al. 2023](#)). From Figure 6 we can see by eye that the recovered process in each time series looks significantly different. The processes recovered to explain FWHM and BIS Span present variations that are shorter than the time sampling of the HARPS data, this behaviour can be a result of overfitting (see [Blunt et al. 2023](#)). We can also see that the recovered signals for S_{HK} and H_α are consistent with a low harmonic complexity process. [Barragán et al. \(2023\)](#) noted that this behaviour can be caused by relatively high white noise that does not allow to characterise the complexity of the underlying signal.

These results suggest that the stellar signal in the activity indicators time series cannot be characterised assuming it behaves as a GP. The rotation period of the star of 3 days is short compared with our sampling strategy of taking one point per night. Three points may not be enough to sample the complexity of the stellar signal, especially if this signal is expected to vary significantly in short time scales, as suggested by the *TESS* photometry. Therefore, our GP regression may not be able to characterise in full the stellar signal. Furthermore, the rotation period of the star is close to the integer of 3 d. This has as a consequence that observations do not sample properly the phase of the stellar rotation given that observations happen at similar times during the whole observing run. This is worsened in the case in which the stellar signal evolves drastically between each period.

We conclude that for our spectroscopic time series, we can constrain the rotation period of the star. However, any further complexity pattern that may exist cannot be characterised by our dataset. Because of this lack of information on the activity indicators, we conclude that this data set is not a good target to perform multi-dimensional GP regression.

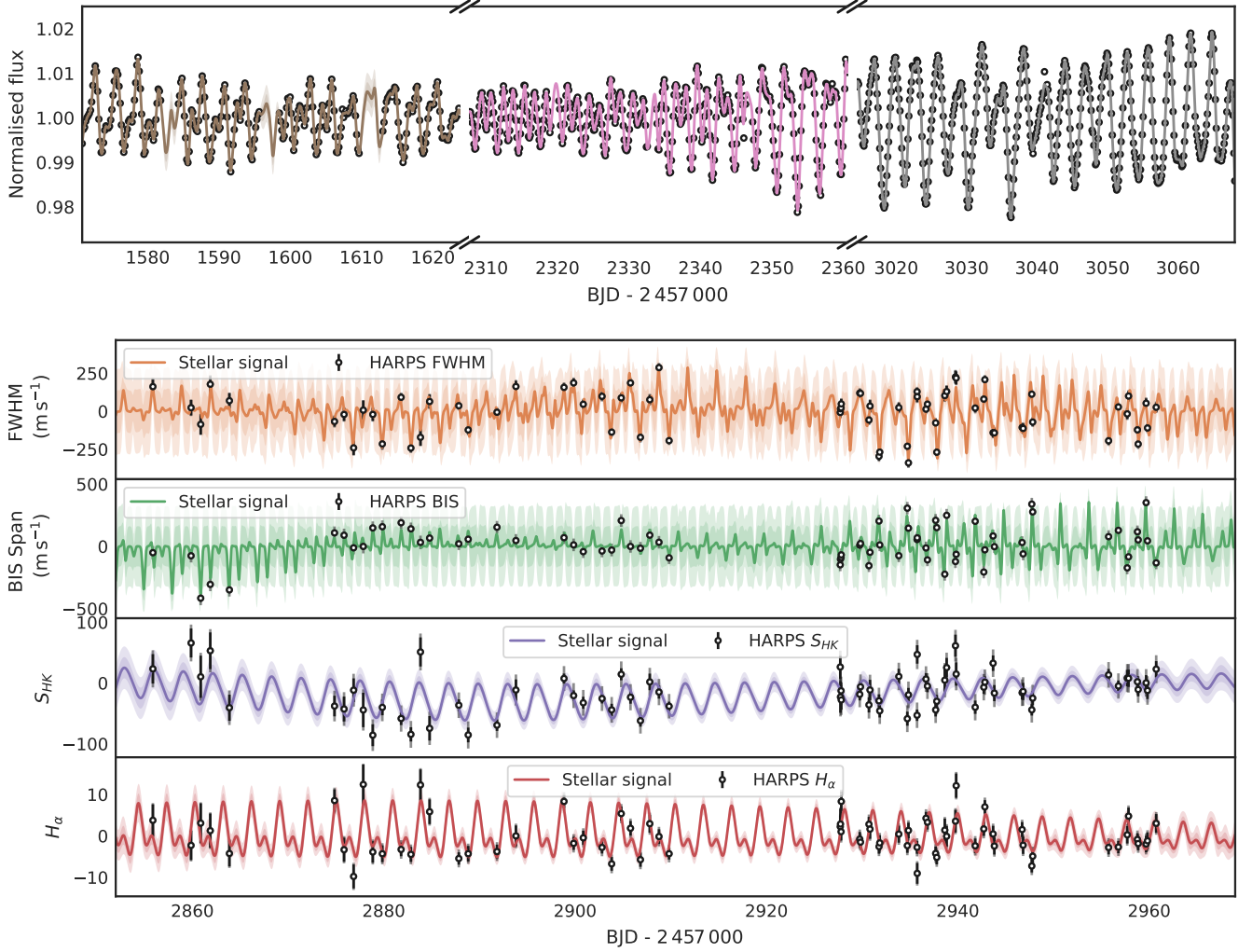


Figure 6. *Top panel:* TOI-837’s TESS light curves and GP inferred models. The corresponding measurements (3 h binned data) are shown with black circles. Solid-coloured lines show the corresponding inferred signal coming from our GP regression for TESS Cycles 1 (brown), 3 (pink), and 5 (grey). *Bottom panel:* TOI-837 spectroscopic time-series for FWHM, BIS Span, S_{HK} , and H_{α} . The corresponding measurements are shown with black circles with error bars with a semi-transparent error bar extension accounting for the inferred jitter. Solid-coloured lines show the corresponding inferred signal coming from our GP regression, while light-coloured shaded areas show the one and two-sigma credible intervals of the corresponding GP model.

3.4 RV analysis

We also performed onedimensional GP modelling to the RVs time series. We first ran a model identical to the GP analyses in Sect. 3.3.2. This means that we sample for the QP kernel hyperparameters (A , P_{GP} , λ_e , λ_p), and a jitter term. As a mean function, we included just an offset (with no Keplerian model yet). For the GP hyperparameters, we use the same priors as the ones described in Sect. 3.3.2. We recover the hyperparameters $P_{GP} = 3.00 \pm 0.02$ d, $\lambda_e = 42^{+25}_{-16}$ d, and $\lambda_p = 0.39^{+0.22}_{-0.13}$. We can see that besides the period, the hyperparameters do not compare with any of the hyperparameters obtained from the other spectroscopic time series (see Table 4).

We then repeated the analysis but this time we added a mean function that includes an offset and a Keplerian model to account for the Doppler effect of TOI-837 b. For the planet model we assume a circular orbit, we set Gaussian priors for the planet ephemeris based on the analysis in Sect. 3.2. For the Doppler semi-amplitude we set a uniform prior between 0 and 100 m s⁻¹. We inferred hyperparameters

fully consistent with the no-planet model; $P_{GP} = 3.00 \pm 0.01$ d, $\lambda_e = 50^{+24}_{-17}$ d, and $\lambda_p = 0.39^{+0.20}_{-0.13}$. We also recovered a Doppler semi-amplitude of $K = 36.6 \pm 6.5$ m s⁻¹. If this signal is caused by TOI-837 b, that would correspond to a planetary mass of $\sim 0.40 M_J$.

When comparing both models, the one with the planetary signal is strongly favoured with a $\Delta AIC = 21$. It is also worth mentioning that the recovered jitter term for the model with the planet signal is 30 m s⁻¹, while with no-planet is 38 m s⁻¹. This is also evidence that the model that better adjusts the data is the one where the planetary signal is included.

3.5 Final joint model

Based on the analyses presented in this section, our final model for the photometric data of TOI-837 is the transit model described in Section 3.2, together with the RV model described in Sect. 3.4. For completeness, we ran a final joint model of photometry and RVs to

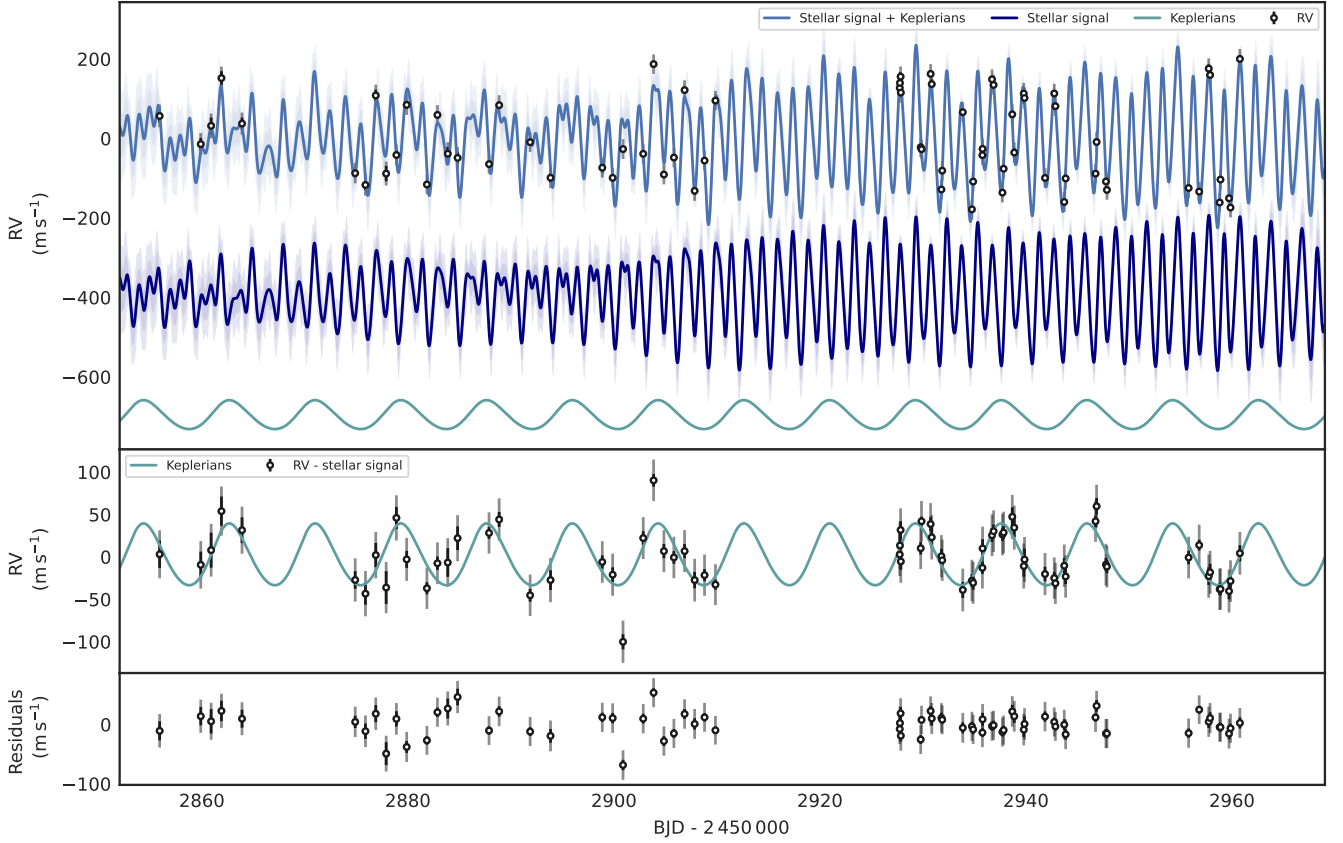


Figure 7. TOI-837’s RV time-series after being corrected by inferred offsets. *Top panel:* RV data together with full, stellar and planetary signal inferred models; RV data with stellar signal model subtracted; and RV residuals. Measurements are shown with black circles, error bars, and a semi-transparent error bar extension accounting for the inferred jitter. The solid lines show the inferred full model coming from our multi-GP, light-shaded areas showing the corresponding GP model’s one and two-sigma credible intervals. We also show the inferred stellar (dark blue line) and planetary (light green line) recovered signals with an offset for better clarity. *Middle panel:* RV data with stellar signal model subtracted and planetary model. *Bottom panel:* RV residuals.

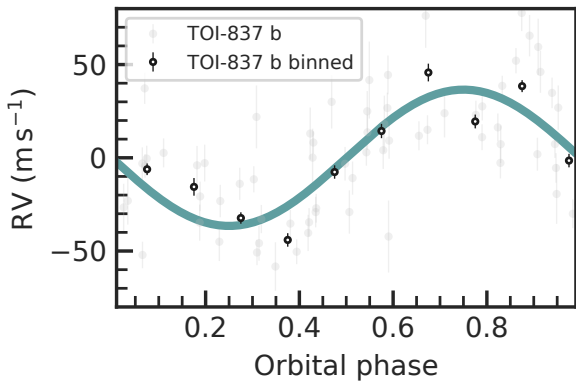


Figure 8. Phase-folded RV signal of TOI-837 b following the subtraction of the systemic velocity and the stellar signal model. The solid line shows the inferred model. Nominal RV observations are shown as light grey points. Solid colourful points show binned data to 1/10 of the orbital phase.

characterise TOI-837 b. The whole set of sampled parameters and priors are shown in Table 3.

We also explored a solution where we allowed for an eccentricity. We inferred an orbital eccentricity of $0.08^{+0.07}_{-0.05}$. However, the model

including a circular orbit is slightly preferred with $\Delta \text{AIC} = 3$. This suggests that the orbit of TOI-837 b is (close to) circular and the data we have is not enough to measure any small deviation from it.

Figure 7 shows the RV time series, while Fig. 8 shows the phase-folded Doppler signal. Table 3 shows the inferred sampled parameters, defined as the median and 68.3% credible interval of the posterior distribution. Table 3 also shows the derived planetary and orbital parameters.

4 DISCUSSION

4.1 RV detection tests

We know a priori that TOI-837 b exists and its nature is consistent with being planetary (B20). Therefore, we expect that there is a Doppler signal larger than zero that is consistent with the ephemeris of the transiting signal. If we assumed that TOI-837 b has the same properties as similar planets with its radius, we estimated a mass of $\sim 0.11 M_J$ that would generate a Doppler signal of $\sim 10 \text{ m s}^{-1}$ (Chen & Kipping 2017). Due to its youth ($\sim 35 \text{ Myr}$), we would expect a rather lower density object with a significantly smaller mass (e.g., Baraffe et al. 2008; Fortney et al. 2007). Our detected Doppler semi-amplitude is $36.2^{+6.8}_{-6.3} \text{ m s}^{-1}$ which translates to a mass of

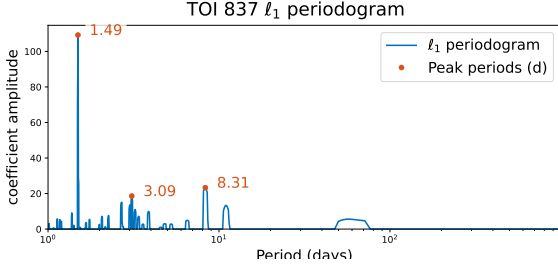


Figure 9. ℓ_1 -periodogram for TOI-837 RVs.

$0.395^{+0.074}_{-0.069} M_J$ for TOI-837 b. This mass together with the inferred radius of $0.817^{+0.032}_{-0.023} R_J$ results in a planetary density of $0.89^{+0.20}_{-0.18} \text{ g cm}^{-3}$. This unexpected high density on young giant planets has been found previously (Suárez Mascareño et al. 2021), but the RV detection of such planets are challenged by the community (e.g., Blunt et al. 2023). In this section, we test the reliability of our detection of the induced Doppler signal on TOI-837.

4.1.1 Planet signal in periodograms

As shown in Section 2.3.1 and Figure 2 there is no evidence of the planetary signal in RV GLS periodogram of TOI-837. This is expected given that any planetary signal would be dwarfed by the relatively high stellar activity signal.

We then took the residuals that we obtained from the no-planet one-dimensional GP analysis presented in Sect. 3.4 and we applied a GLS periodogram that is shown in the bottom panel of Figure 2. We can see that the peaks that correspond to the stellar signal disappeared from the periodogram, indicating that the GP model was able to remove the intrinsic stellar signal in the RV time series. Furthermore, a significant peak appeared close to the orbital period of the planet. This result is unexpected. GPs have been proven to engulf planetary signals, especially when the latter ones are not included in the model (e.g., Ahner et al. 2021; Rajpaul et al. 2021). We speculate that if a relatively strong coherent signals is present in our data set, it may survive a GP regression if it evolves with significantly different time scales than the stellar signal. This assumption is consistent with the recovered Doppler signal of TOI-837 b.

To explore further the existence of the planetary signal in the periodogram, we ran a ℓ_1 periodogram (Hara et al. 2017) on the raw RV time series. Briefly, the ℓ_1 -periodogram is a variation of the Lomb-Scargle periodogram methodology that has reduced sensitivity towards outliers and non-Gaussian noise. Figure 9 shows the ℓ_1 -periodogram applied to the raw RV time-series of TOI-837. The three most significant peak happens at 1.5, 8.31 and 3.09 d that correspond to the first harmonic of the rotation period of the star, the planet orbit, and the rotation period of the star, respectively. This suggests that there is a strong deep-seated signal that coincides with the orbital period of TOI-837 b. This result supports our previous speculation that there is evidence of strong coherent signal in the RVs that is consistent with our TOI-837 b's recovered Doppler signal.

4.1.2 Cross-validation

The next test we perform is cross-validation to check for overfitting as suggested by Blunt et al. (2023). To do so, we employ a data partitioning strategy similar to the principles of k-fold cross-validation (see e.g., Fazekas & Kovacs 2024) to systematically divide our dataset

into distinct subsets. Specifically, we first randomised the dataset to ensure that each partition is representative of the overall data distribution. Subsequently, we segmented the dataset into five partitions. In each iteration, we use four out of these five partitions (constituting approximately 80% of the data) for the modelling, while the remaining partition (approximately 20% of the data) is masked out. This approach guarantees that each unique subset serves as the test set exactly once, eliminating any potential overlap between masked-out data across all iterations. Figure 10 shows the five different sub-samples created with this approach.

We then perform a RV analysis (accounting for the planet signal) as the one presented in Sect. 3.4 for each sub-sample, we call each one of these runs as sub-test i , where i runs between 1 and 5. Figure 10 shows the data and recovered model for all cases. The recovered Doppler semi-amplitude for each case is fully consistent with the value reported in Sect. 3.4, but with slightly larger error bars, as expected due to the smaller number of data modelled. We can see that, by eye, the masked-out points fall well within the limits of the inferred models in each case, suggesting that the predictive model in each case can explain the masked-out observations (see also discussion in Luque et al. 2023). We can also see that the predictive model for each sub-set (black lines) falls well within the confidence intervals of the predictive distribution of the model of the full data set (blue lines and shaded region). These results suggest that our model does not suffer overfitting.

To assess further the reliability of our cross-validation, we perform a Two-sample Kolmogorov-Smirnov (KS; Kolmogorov 1933; Smirnov 1948) test. Briefly, the KS test is a non-parametric statistical test that is utilised to validate the hypothesis that two subsets of data originate from the same continuous distribution. This test compares the empirical cumulative distribution functions (ECDFs) of two samples without making any assumptions about the underlying distribution of data. The maximum absolute difference between the ECDFs of the two samples, known as the KS statistic, serves as the basis for evaluating the null hypothesis that the two samples are drawn from the same distribution. A low KS statistic, accompanied by a high p-value, indicates a failure to reject the null hypothesis, suggesting that the differences between the two samples could be attributed to random variation, and hence, they can be considered as coming from the same distribution.

We apply the KS test to each one of our sub-tests in which we compare the residuals of the modelled data with the residuals of the masked-out data (i.e., masked-out points minus predictive distribution at their respective times). If the KS test proves that both samples are explained from the same distribution, then we can conclude that the predictive model explains well the masked-out data. This implies that the inferred model has the ability to explain unseen data, thus, it does not overfit. Figure 10 shows the ECDF for the modelled and masked-out data for each one of the sub-tests. The p-values of the five sub-tests are significantly larger than 0.05, therefore, we can conclude that both samples are consistent with being described by the same underlying distribution. These results give us confidence that our RV model for TOI-837 does not suffer from overfitting.

4.1.3 Injection tests

Previous research indicates that complex models can generate false planet-like RV time series, particularly in stars with high activity levels (e.g., Rajpaul et al. 2016). To check if this is our case, we performed injection tests similar to the ones presented in Barragán et al. (2019b); Zicher et al. (2022). We used citlalatonac (Barragán et al. 2022a) to simulate synthetic RV time series at the same

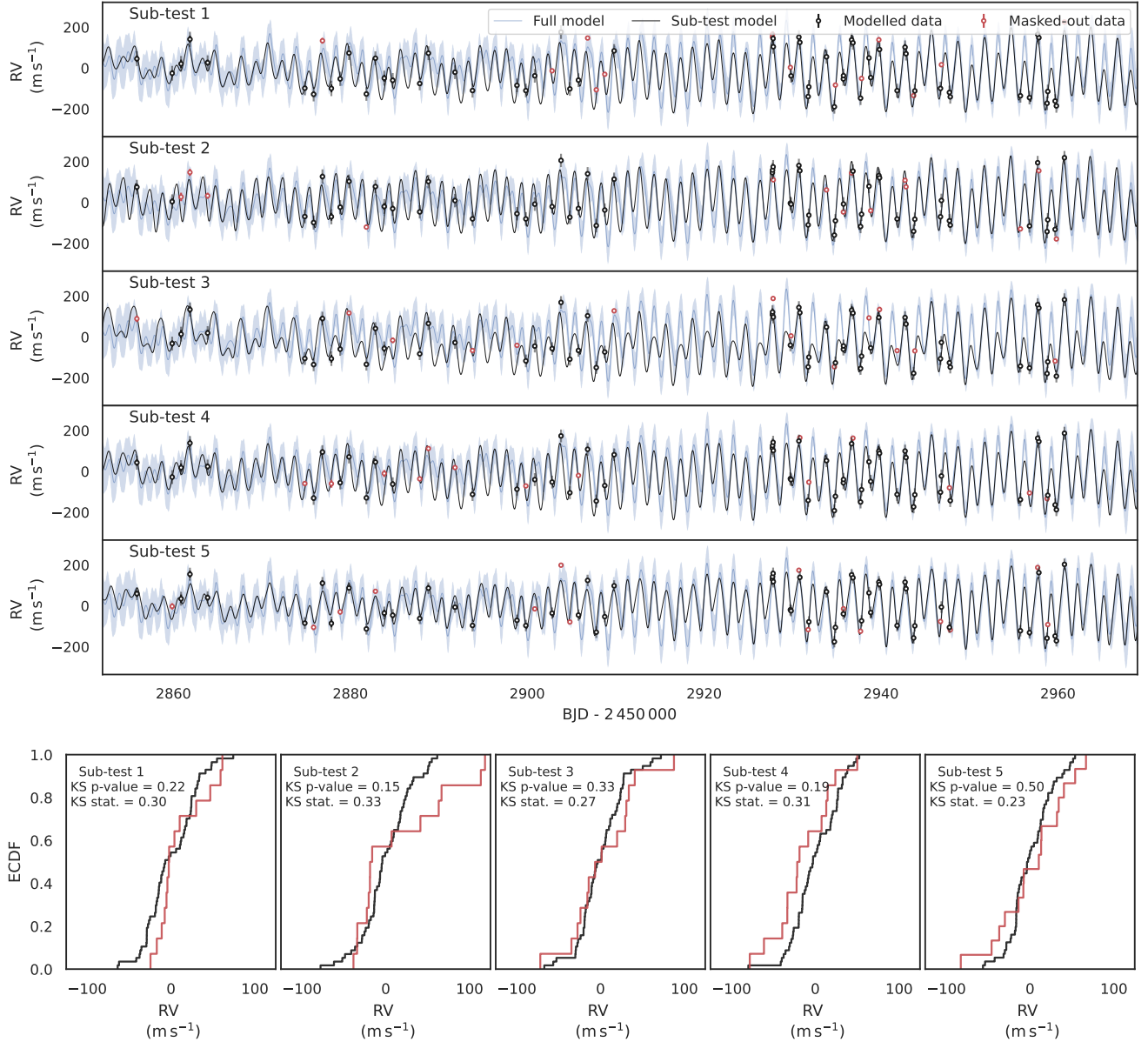


Figure 10. *Top panel:* Cross-validation results with RV data sub-sets. Dark circles represent modelled data, red circles indicate masked-out data. Black solid line shows the recovered model for each sub-test. We also show the full model and $3 - \sigma$ confidence interval of the full model recovered from the whole data set (same inferred model as Figure 7) with a blue line and light shaded areas, respectively. *Bottom panel:* Empirical Cumulative Distribution Functions (ECDF) for the residuals of the modelled (black) and masked-out (red) data for all sub-tests. Each sub-plot shows the corresponding KS statistics.

time-stamps as our HARPS data. We first took the predictive distribution for the stellar signal that we obtained for TOI-837 in Sect. 3.4. We then added correlated noise using a squared exponential kernel with a length scale of one day, and the same amplitude as the jitter term obtained from the real data to simulate the red noise in our data. To finish, we also added white noise for each synthetic observation according to the nominal measurement uncertainty of each HARPS datum. We created 100 different realisations of stellar-like signals. For each stellar-like signal, we created 3 different types of RV time series injecting signals with Doppler semi-amplitudes of 0 (assuming there is no planet), 10 (expected signal of this planet if it were inflated), and 36 m s^{-1} (the recovered signal). This leads to a total of 300 synthetic RV time series with similar noise properties and the same time sampling as the real data.

We model each synthetic dataset using a one-planet model and onedimensional GP configuration as described in Sect. 3.4. We plot the recovered posterior distribution of the Doppler semi-amplitude of the planet for all the runs in Figure 11.

We first check the percentage of the simulations in which we can claim a detection. For this purpose, we consider that a detection has occurred if the median of the posterior is larger than $3 - \sigma$, where σ is half the interval between the 16.5th and 83.5th percentiles. We found that we can claim a detection of 4%, 28%, and 100% for the synthetic time series with injected signals of 0, 10, and 36 m s^{-1} , respectively. We then revise which percentage of these detections is consistent with our detection in the real data set. We check what fraction of the time the recovered semi-amplitude in the synthetic time series is within $1 - \sigma$ of the recovered posterior distribution

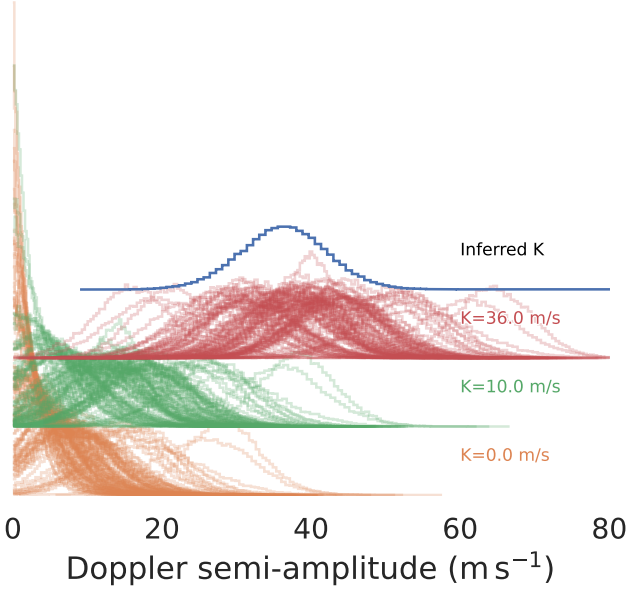


Figure 11. Doppler semi-amplitude distributions from injection tests. The blue line shows results from original data; other coloured lines from synthetic data. Labels indicate injected values.

from the real data set. We found that this condition is filled in 0%, 2%, and 55% of the cases for the 0, 10, and 36 m s^{-1} time series, respectively. These results suggest that if the real Doppler signal presented in our RV time-series was 10 m s^{-1} we would detect the 36 m s^{-1} signal with a probability of 2%. The 55% recovered in the 36 m s^{-1} case is consistent with the expected value taking into account Poisson counting errors.

For the remainder of the paper, we will assume that our mass and radius measurements of TOI-837 b are reliable. Below we describe the physical implications of this for the planet’s properties.

4.2 TOI-837b’s properties

With a mass of $0.395^{+0.074}_{-0.069} M_J$ and radius of $0.817^{+0.032}_{-0.023} R_J$, TOI-837 b’s position in the mass-radius diagram is highlighted in Fig. 12. Figure 12 also shows a mass-radius diagram for giant exoplanets ($0.5 < R_J < 2 R_J$ and $0.1 < M_p < 5 M_J$) detected with a precision better than 30% in radius and mass. Considering that the evolution of planets is influenced by their distance from their host star, we only present planets that orbit within a semi-major axis range of 0.08 to 1 AU. This selection is informed by the semi-major axis of TOI-837 b, ~ 0.09 AU, and is supported by models that forecast a comparable evolution for planets situated within this range of semi-major axes (see Fortney et al. 2007). We also over plot the Fortney et al. (2007)’s models with similar parameters to those of TOI-837 b. This corresponds to models for planets around a solar-like star, with an age of 32 Myr, at a distance of 0.1 AU with cores of 25 (pink), 50 (orange) and 100 (green) M_\oplus . We performed a radial basis function interpolation on the aforementioned Fortney et al. (2007)’s models to find the core mass that best describes the mass and radius of TOI-837 b. We found that the position and age of TOI-837 b would be consistent with a young planet with a core mass of 71 M_\oplus , assuming

a 50-50% ice-silicate core (black line in Fig. 12). This core mass corresponds to $\sim 60\%$ of TOI-837 b total mass of $\sim 125 M_\oplus$.

From figure 12, we can see that if well there are planets that fall close to TOI-837 b in the mass vs radius diagram, they all are older than 1 Gyr and they should be compared with older planet’s models. This can be done from figure 12 where we also show the Fortney et al. (2007)’s models for planets aged 3 Gyr with orbital semi-major axis of 0.1 AU. The first thing we see is that the older counterparts of TOI-837 b are consistent with planets with cores $\lesssim 50 M_\oplus$. If TOI-837 b itself was older, we would estimate a significantly smaller core of $\sim 50 M_\oplus$, our estimation of $\sim 70 M_\oplus$ is a pure consequence of the expected inflated state, hence larger radius, given its youth. In this line of thought, TOI-837 b stands out as the only planet with a semi-major axis of ~ 0.1 AU consistent with a $\sim 70 M_\oplus$ core.

We then relaxed our assumptions and proceed to compare TOI-837 b with planets with similar mass and radius, but without constrain on their semi-major axes. We found that K2-60 b (Eigmüller et al. 2017), HD 149026 b (Sato et al. 2005), and TOI-1194 b (Wang et al. 2023) are denser than TOI-837 b and are consistent with core masses between 50–100 M_\oplus despite being significantly older (> 1 Gyr). This suggests that planets with relatively similar masses to TOI-837 b and large cores can exist. The question now is what physical mechanisms can create such massive cores. Johnson & Li (2012) theorised that a star’s high metallicity might reflect a primordial circumstellar disc with elevated dust content that could potentially enhance core formation. Both, HD 149026 b and TOI-1194 b have super-solar atmospheric metallicities that are consistent with this model. In fact, Bean et al. (2023) observed a significant atmospheric metal enrichment on the atmosphere of HD 149026 b that is explained by a bulk heavy element abundance of 66% of the planetary mass. However, the solar metallicity of TOI-837 and K2-60 does not support this hypothesis, suggesting that other factors may also play a critical role in the formation of massive cores. Boley et al. (2016) proposed a theory where massive cores, with masses exceeding 20 M_\oplus , could result from the merging of tightly packed orbiting inner planets that formed during the initial phases of the circumstellar disc’s evolution.

Another possibility is that TOI-837 b has a less massive core, but the models are biased towards larger radii for young planets. Core-accretion models of planetary evolution predict planets of < 100 Myr to be at the early stages of their contraction phase, showing very large radii and low densities (Baraffe et al. 2008; Fortney et al. 2007, see also 1 Myr models in Fig. 12). However, Fortney et al. (2007)’s models do not include a formation mechanism and can be arbitrarily large and hot at very young ages (see Marley et al. 2007). This can lead to giant planet’s models with radii several tenths of a Jupiter radius larger than one computed taking into account formation mechanisms. This would lead as a consequence to estimate more massive cores for a given planet’s mass and radius.

For the remainder of the paper we will assume that TOI-837 b can be described by Fortney et al. (2007)’s models assuming a core of 70 M_\oplus .

4.3 Atmospheric characterisation perspectives

Atmospheric observations could play a crucial role in differentiating among various potential formation mechanisms for TOI-837 b. According to the mass-metallicity relationship empirically established by Thorngren et al. (2016), our mass measurement of TOI-837 b suggests a predicted metal fraction ratio between the planet and its host star of $Z_{\text{planet}}/Z_{\text{star}} = 14.7 \pm 2.5$. With TOI-837’s stellar metallicity measured at $[\text{Fe}/\text{H}] = 0.01 \pm 0.04$, this translates into an estimated

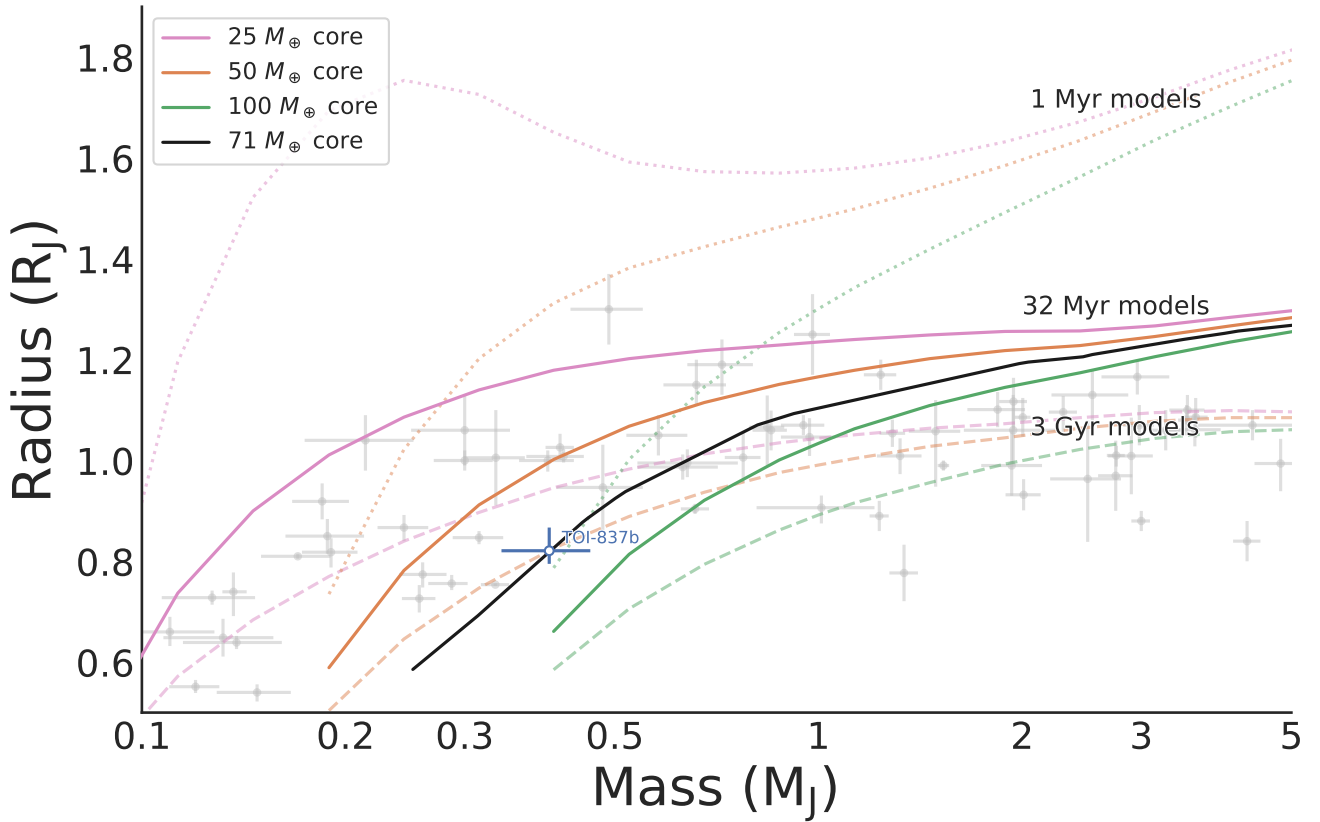


Figure 12. Mass vs Radius Diagram. Grey data points with error bars show exoplanets with mass and radius measurements with a precision of 30% or better and orbital semi-major axis between 0.08 and 1 AU. Data taken from the NASA Exoplanet Archive as of March 2024 (<https://exoplanetarchive.ipac.caltech.edu/>; Akeson et al. 2013). The location of TOI-837 b is highlighted by a blue circle. Solid lines depict theoretical models predicting the mass-radius relationship for planets of varying core masses, assuming an age of 32 Myr and a distance of 0.1 AU from a Sun-like star, based on Fortney et al. (2007). Dotted and dashed lines extend these predictions to planets aged 1 Myr and 3 Gyr, respectively. Black line shows the interpolated model for a 32 Myr old and $71 M_{\oplus}$ core. Jupiter and Saturn are shown with their respective astronomical symbols. The methodology for generating this diagram follows the approach outlined in Barragán et al. (2018).

bulk metallicity fraction for TOI-837 b of 0.21 ± 0.04 . Bean et al. (2023) presents a relationship between atmospheric and bulk metallicity fractions. If we assume that TOI-837 b follows this trend, we could expect its atmospheric metallicity to surpass solar values by a factor of 5 – 8. This significant enhancement in atmospheric metallicity would not only support the substantial core mass inferred from our observations but also provide insight into the planet’s formation conditions and subsequent evolutionary history.

To predict the observability of the atmosphere of TOI-837 b with *JWST*, we leverage packages *PICASO*⁵ and *PANDEXO*⁶. We forward model the emission spectrum of TOI-837 b using *PICASO* (Batalha et al. 2019), based on the parameters derived in this work. We make use of the integrated 1D climate modelling for the temperature-pressure (TP) profile and chemical abundance solution (Mukherjee et al. 2023), including all opacities available in *PICASO*. The TP profile includes a convective zone only in the deepest atmospheric layers. We then use *PANDEXO* to estimate the signal-to-noise of the dayside emission signal of TOI-837 b with *JWST/NIRSpec G395H*; the predicted observations using three eclipses are shown in Fig. 13, assuming solar metallicity and C/O. At least two eclipse observations

are needed to distinguish between a $1\times$ and $10\times$ solar metallicity scenario. Using the chi-square statistic for hypothesis testing, we would expect to distinguish between these cases to a significance of 11.1σ with two eclipse observations (totalling 10.01 hrs), rising to 17.1σ with three eclipses (Fig. 13). Constraining the atmospheric metallicity will help to break the degeneracy with interior composition and the implications for formation.

5 CONCLUSIONS

Our investigation into the TOI-837 system and its intriguing companion, TOI-837 b, unveils a young Saturn-sized exoplanet that defies conventional expectations with its unexpected massive core. Our exhaustive analysis of data from *TESS* ground-based observations, and HARPS spectroscopic enabled us to determine TOI-837 b’s radius at $0.817^{+0.032}_{-0.023} R_J$ and mass at $0.395^{+0.074}_{-0.069} M_J$, translating to a density of $0.89^{+0.20}_{-0.18} \text{ g cm}^{-3}$. This density together with its age and distance to the star suggest a core mass of approximately $70 M_{\oplus}$, accounting for 60% of the planet’s total mass. Such a substantial core within a relatively young planetary body presents a challenging scenario for current models of planet formation and core accretion, especially due to the relatively low stellar metallicity.

The unique characteristics of TOI-837 b underscore the urgency

⁵ <https://natashabatalha.github.io/picasso/>

⁶ <https://natashabatalha.github.io/PandExo/index.html>

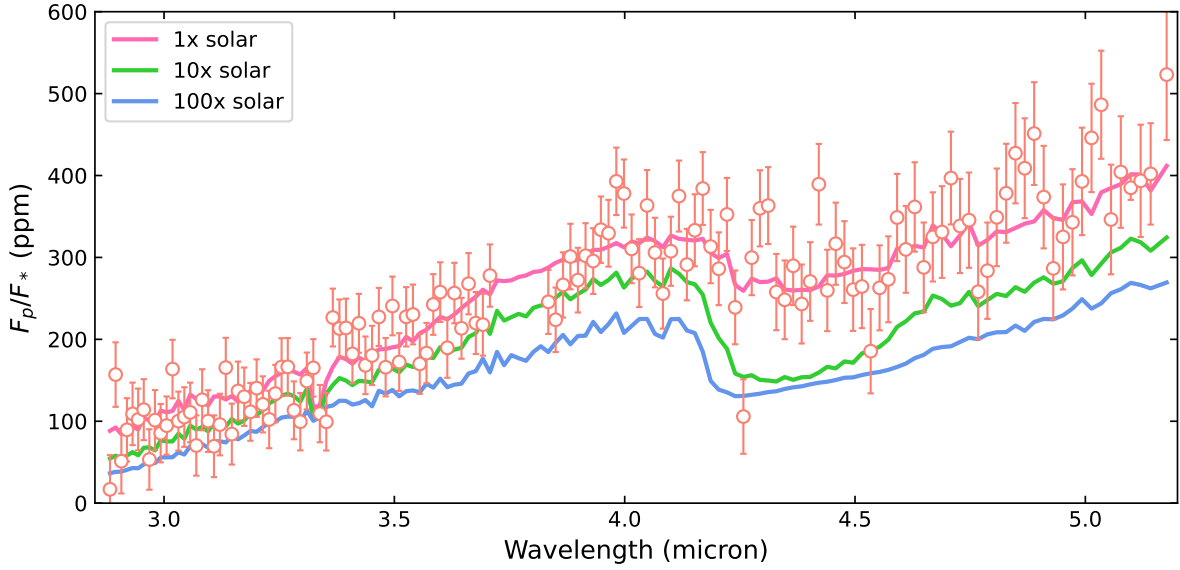


Figure 13. The predicted emission spectrum of TOI-837 b. The red data points show the spectrum attainable with three eclipse observations, using JWST/NIRSpec G395H, assuming a solar composition in both metallicity and C/O ratio. For comparison, the forward-modelled spectra assuming 10× and 100× metallicity are also shown (with solar C/O).

for advanced atmospheric characterisation. Eclipse observations with *JWST* could offer unparalleled insights into the composition of TOI-837 b. A measurement of the planetary atmospheric bulk metal fraction will potentially elucidate the true nature of its significant core. Such future studies are crucial for breaking the current degeneracies in planet composition models and could revolutionise our understanding of planetary formation.

We also leave open the possibility that our RV detection could not be accurate. Despite the tailored campaign with a high cadence of observations, the apparent fast evolution of the strong stellar signal could generate biased measurements of the Doppler semi-amplitude. We showed with several statistical tests that our RV planetary detection is robust, nevertheless, further observations could help us to test this further. For example, tailored near Infrared RV campaigns, where stellar activity is less significant, with instruments such as the Near Infra Red Planet Searcher (NIRPS) could help to assert our detection in the optical.

ACKNOWLEDGEMENTS

This publication is part of a project that has received funding from the European Research Council (ERC) under the European Union’s Horizon 2020 research and innovation programme (Grant agreement No. 865624). This work made use of *numpy* (Harris et al. 2020), *matplotlib* (Hunter 2007), and *pandas* (pandas development team 2020) libraries. This work made use of *Astropy*:⁷ a community-developed core Python package and an ecosystem of tools and resources for astronomy (Astropy Collaboration et al. 2013, 2018, 2022). This publication made use of data products from the Wide-field Infrared Survey Explorer, which is a joint project of the University of California, Los Angeles, and the Jet Propulsion Laboratory/California Institute of Technology, funded by the National

Aeronautics and Space Administration. AVF acknowledges the support of the IOP through the Bell Burnell Graduate Scholarship Fund. OB acknowledges that the random seed used for the injection simulations was 060196.

DATA AVAILABILITY

The codes used in this manuscript are freely available at <https://github.com/oscaribv>. The spectroscopic measurements that appear in Table 2 are available as supplementary material in the online version of this manuscript. All *TESS* data are available via the MAST archive. Ground-based photometry are available on the online version of Bouma et al. (2020).

REFERENCES

- Ahrer E., et al., 2021, *MNRAS*, **503**, 1248
- Aigrain S., Foreman-Mackey D., 2023, *ARA&A*, **61**, 329
- Aigrain S., Pont F., Zucker S., 2012, *MNRAS*, **419**, 3147
- Akeson R. L., et al., 2013, *PASP*, **125**, 989
- Ambikasaran S., Foreman-Mackey D., Greengard L., Hogg D. W., O’Neil M., 2015, *IEEE Transactions on Pattern Analysis and Machine Intelligence*, **38**, 252
- Astropy Collaboration et al., 2013, *A&A*, **558**, A33
- Astropy Collaboration et al., 2018, *AJ*, **156**, 123
- Astropy Collaboration et al., 2022, *ApJ*, **935**, 167
- Baraffe I., Chabrier G., Barman T., 2008, *A&A*, **482**, 315
- Barragán O., et al., 2018, *A&A*, **612**, A95
- Barragán O., Gandolfi D., Antoniciello G., 2019a, *MNRAS*, **482**, 1017
- Barragán O., et al., 2019b, *MNRAS*, **490**, 698
- Barragán O., Aigrain S., Gillen E., Gutiérrez-Canales F., 2021, *Research Notes of the AAS*, **5**, 51
- Barragán O., Aigrain S., Rajpaul V. M., Zicher N., 2022a, *MNRAS*, **509**, 866
- Barragán O., et al., 2022b, *MNRAS*, **514**, 1606
- Barragán O., et al., 2023, *MNRAS*, **522**, 3458

⁷ <http://www.astropy.org>

- Batalha N. E., Lewis T., Fortney J. J., Batalha N. M., Kempton E., Lewis N. K., Line M. R., 2019, *ApJ*, **885**, L25
- Bean J. L., et al., 2023, *Nature*, **618**, 43
- Blanco-Cuaresma S., 2019, *MNRAS*, **486**, 2075
- Blunt S., et al., 2023, *AJ*, **166**, 62
- Boley A. C., Granados Contreras A. P., Gladman B., 2016, *ApJ*, **817**, L17
- Bouma L. G., et al., 2020, *AJ*, **160**, 239
- Chen J., Kipping D., 2017, *ApJ*, **834**, 17
- Cretignier M., 2022, PhD thesis, University of Geneva, Switzerland
- Cretignier M., Dumusque X., Allart R., Pepe F., Lovis C., 2020a, *A&A*, **633**, A76
- Cretignier M., Francfort J., Dumusque X., Allart R., Pepe F., 2020b, *A&A*, **640**, A42
- Cretignier M., Dumusque X., Hara N. C., Pepe F., 2021, *A&A*, **653**, A43
- Cutri R. M., et al., 2003, VizieR Online Data Catalog, p. II/246
- David T. J., et al., 2018, *AJ*, **155**, 222
- Dotter A., 2016, *ApJS*, **222**, 8
- Doyle A. P., Davies G. R., Smalley B., Chaplin W. J., Elsworth Y., 2014, *MNRAS*, **444**, 3592
- Eigmüller P., et al., 2017, *AJ*, **153**, 130
- Fazekas A., Kovacs G., 2024, *arXiv e-prints*, p. arXiv:2401.13843
- Feroz F., Hobson M. P., Cameron E., Pettitt A. N., 2019, *The Open Journal of Astrophysics*, **2**, 10
- Foreman-Mackey D., Hogg D. W., Lang D., Goodman J., 2013, *PASP*, **125**, 306
- Fortney J. J., Marley M. S., Barnes J. W., 2007, *ApJ*, **659**, 1661
- Freckelton A. V., Sebastian D., Mortier A., Triaud A., et al., 2024, submitted to MNRAS
- Gaia Collaboration 2020, VizieR Online Data Catalog, p. I/350
- Gandolfi D., et al., 2018, *A&A*, **619**, L10
- Gregory P. C., 2005, *ApJ*, **631**, 1198
- Guerrero N. M., et al., 2021, *ApJS*, **254**, 39
- Gustafsson B., Edvardsson B., Eriksson K., Jørgensen U. G., Nordlund Å., Plez B., 2008, *A&A*, **486**, 951
- Hara N. C., Boué G., Laskar J., Correia A. C. M., 2017, *MNRAS*, **464**, 1220
- Harris C. R., et al., 2020, *Nature*, **585**, 357
- Hobson M. J., et al., 2021, *AJ*, **161**, 235
- Høg E., et al., 2000, *A&A*, **355**, L27
- Howell S. B., et al., 2014, *PASP*, **126**, 398
- Hunter J. D., 2007, *Computing in Science & Engineering*, **9**, 90
- Jenkins J. M., 2002, *ApJ*, **575**, 493
- Jenkins J. M., et al., 2010, in Radziwill N. M., Bridger A., eds, Society of Photo-Optical Instrumentation Engineers (SPIE) Conference Series Vol. 7740, Software and Cyberinfrastructure for Astronomy. p. 77400D, doi:10.1117/12.856764
- Jenkins J. M., et al., 2016, in Proc. SPIE. p. 99133E, doi:10.1117/12.2233418
- Jenkins J. M., Tenenbaum P., Seader S., Burke C. J., McCauliff S. D., Smith J. C., Twicken J. D., Chandrasekaran H., 2020, Kepler Data Processing Handbook: Transiting Planet Search, Kepler Science Document KSCI-19081-003
- Johnson J. L., Li H., 2012, *ApJ*, **751**, 81
- Kipping D. M., 2013, *MNRAS*, **435**, 2152
- Kolmogorov A., 1933, *G. Ist. Ital. Attuari*, **4**, 83
- Kurucz R. L., 1993, SYNTHES spectrum synthesis programs and line data. Kurucz CD-ROM
- Li J., Tenenbaum P., Twicken J. D., Burke C. J., Jenkins J. M., Quintana E. V., Rowe J. F., Seader S. E., 2019, *PASP*, **131**, 024506
- Lovis C., 2007, PhD thesis, University of Geneva, Switzerland
- Luque R., et al., 2023, *Nature*, **623**, 932
- Mallorquín M., et al., 2023, *A&A*, **680**, A76
- Mandel K., Agol E., 2002, *ApJ*, **580**, L171
- Mann A. W., et al., 2021, *arXiv e-prints*, p. arXiv:2110.09531
- Mantovan G., et al., 2023, *arXiv e-prints*, p. arXiv:2310.16888
- Marley M. S., Fortney J. J., Hubickyj O., Bodenheimer P., Lissauer J. J., 2007, *ApJ*, **655**, 541
- Martoli E., Hébrard G., Correia A. C. M., Laskar J., Lecavelier des Etangs A., 2021, *A&A*, **649**, A177
- Mayor M., et al., 2003, *The Messenger*, **114**, 20
- Mortier A., et al., 2020, *MNRAS*, **499**, 5004
- Morton T. D., 2015, VESPA: False positive probabilities calculator, Astrophysics Source Code Library (ascl:1503.011)
- Mukherjee S., Batalha N. E., Fortney J. J., Marley M. S., 2023, *ApJ*, **942**, 71
- Rajpaul V., Aigrain S., Osborne M. A., Reece S., Roberts S., 2015, *MNRAS*, **452**, 2269
- Rajpaul V., Aigrain S., Roberts S., 2016, *MNRAS*, **456**, L6
- Rajpaul V. M., et al., 2021, *MNRAS*, **507**, 1847
- Ricker G. R., et al., 2015, *Journal of Astronomical Telescopes, Instruments, and Systems*, **1**, 014003
- Rizzuto A. C., et al., 2020, *AJ*, **160**, 33
- Sato B., et al., 2005, *ApJ*, **633**, 465
- Smirnov N., 1948, *The Annals of Mathematical Statistics*, **19**, 279
- Smith J. C., et al., 2012, *PASP*, **124**, 1000
- Southworth J., Wheatley P. J., Sams G., 2007, *MNRAS*, **379**, L11
- Stumpe M. C., et al., 2012, *PASP*, **124**, 985
- Stumpe M. C., Smith J. C., Catanzarite J. H., Van Cleve J. E., Jenkins J. M., Twicken J. D., Girouard F. R., 2014, *PASP*, **126**, 100
- Suárez Mascareño A., et al., 2021, *Nature Astronomy*, **6**, 232
- Thorngren D. P., Fortney J. J., Murray-Clay R. A., Lopez E. D., 2016, *ApJ*, **831**, 64
- Tsantaki M., Sousa S. G., Adibekyan V. Z., Santos N. C., Mortier A., Israelian G., 2013, *A&A*, **555**, A150
- Tsantaki M., Andreasen D., Teixeira G., 2020, *Journal of Open Source Software*, **5**, 2048
- Twicken J. D., et al., 2018, *PASP*, **130**, 064502
- Wang J.-Q., et al., 2023, *arXiv e-prints*, p. arXiv:2310.12458
- Winn J. N., 2010, *arXiv e-prints*, p. arXiv:1001.2010
- Zechmeister M., Kürster M., 2009, *A&A*, **496**, 577
- Zicher N., et al., 2022, *MNRAS*, **512**, 3060
- pandas development team T., 2020, pandas-dev/pandas: Pandas, doi:10.5281/zenodo.3509134, https://doi.org/10.5281/zenodo.3509134

This paper has been typeset from a \LaTeX file prepared by the author.